Flocking Phase Separation in Inertial Active Matter

Nan Luo, 1,2,* Longfei Li, 1,4 Mingcheng Yang, 1,2,† and Yi Peng, 1,2,‡

Beijing National Laboratory for Condensed Matter Physics and Laboratory of Soft Matter Physics, Institute of Physics,

Chinese Academy of Sciences, Beijing 100190, China

School of Physical Sciences, University of Chinese Academy of Sciences, Beijing 100049, China

(Received 19 February 2025; accepted 29 September 2025; published 21 October 2025)

A large population of motile agents can display remarkable collective behaviors. Here, we study collective motion of inertia-dominated macroscopic agents using a model system of millimeter-sized magnetic rollers with tunable motile behaviors. In this system, we observe first-order flocking phase separation, where a uniform flock propagates through an isotropic gaseous phase. The flocking phase and the coexisting gaseous phase exhibit distinct particle exchange dynamics and maintain different effective temperatures, which are unattainable in equilibrium systems. Combining experiments, agent-based simulations, and phenomenological theories, we demonstrate that inelastic collisions between inertial and externally driven magnetic rollers produce positive feedback between high density and polar motion, driving flocking phase separation. Our Letter reveals a novel mode of collective motion in inertial active matter, with potential implications for controlling biological flocks and designing robotic swarms.

DOI: 10.1103/hb7b-wp95

Introduction—Active matter comprises agents that propel themselves with energy input at individual scales [1-3]. Populations of motile agents self-organize into complex structures and move collectively [4], with broad implications for animal flocks [5] and robot swarms [6-9]. However, despite their considerable biological and technological importance, the principles of collective motion remain poorly understood largely because of complicated motile behaviors and interagent interactions. A productive approach to studying collective motion is to build artificial model systems with simplified interaction and controllable motility. Prominent examples include Quincke rollers [10] and self-propelled Janus particles [11], which represent microscopic active matter exhibiting overdamped dynamics. In contrast, the inertia of macroscopic agents significantly impacts the motion by introducing finite acceleration time, governing collisions, and dragging ambient fluids. Recent studies show inertial motile agents exhibit a number of remarkable phenomena in intermediate-Reynoldsnumber fluids [12–16]. Examples of macroscopic motile agents in fluid-free environments, such as self-propelled granular particles on a vibrating bed [17] and microbots [18,19], experience approximately overdamped motion due to strong energy dissipation induced by frictional substrates. The collective motion of inertial dry agents has been rarely explored experimentally, although simulations suggest that inertia introduces novel features in collective behaviors [20,21].

Here, we develop a model system consisting of magnetic rollers for inertial dry active matter with tunable motility, driven by a magnetic field. We observe that an isotropic roller assembly becomes unstable above a certain concentration threshold, and phase-separates into two uniform coexisting phases with sharp interfaces via nucleation: a dilute disordered phase and a dense, fast-moving flock. In general, this flocking phase separation results from positive feedback between high density and large polar velocity, which is induced by inelastic collisions between inertial rollers driven by the magnetic field. This novel type of phase separation is reminiscent of but fundamentally different from the well-known motility-induced phase separation, where slow particles accumulated in dense regions [22–24].

Single magnetic roller—To incorporate inertial effects in macroscopic motile agents, we develop a controllable active granular system. Our system is composed of numerous ferromagnetic spheres (diameter d=0.5 mm, magnetic dipole moment $m_0=4\times 10^{-7}$ Am²) placed on a horizontal substrate and subjected to a vertical alternating current magnetic field $\mathbf{B}(t)$ (magnitude B=4 mT, period $\tau=1/f$, square wave). See Supplemental Material (SM) for more details [25]. The magnetic dipole, which tends to align with \mathbf{B} , is unstable to infinitesimal fluctuations and rotates when it becomes antiparallel with \mathbf{B} [Fig. 1(a)]. Consequently, the sphere rolls in a random horizontal direction because of friction with the substrate. After realigning with \mathbf{B} , the sphere persists rolling due to inertia until the aligning torque halts its rotation, after which it

^{*}These authors contributed equally to this work.

[†]Contact author: mcyang@iphy.ac.cn ‡Contact author: pengy@iphy.ac.cn

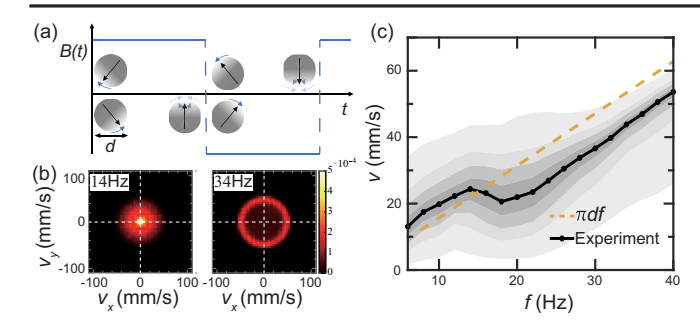


FIG. 1. (a) Schematic illustrating the self-propulsion mechanism of a magnetic roller driven by a vertical square-wave magnetic field. Black arrows indicate the magnetic dipole orientations of the rollers, while blue arrows depict their rotational alignment with the instantaneous external field. (b) Probability distribution of velocity (v) at 14 Hz (left) and 34 Hz (right). (c) Instantaneous speed of an isolated particle. The black line represents median speed, with the gray shading indicating the central 20%, 40%, 60%, and 90% percentiles. The dashed line denotes the reference speed πdf .

rolls back and oscillates. The rolling oscillation continues until the next flip of B. The sphere may move forward or backward in the subsequent half-period, depending on the direction of the magnetic dipole at the moment of flipping. Thus, by adjusting the frequency f, we can tune the motile behaviors of the magnetic rollers. At low frequencies (f < 25 Hz), rollers move in a run-and-oscillate mode with large velocity variation [Fig. 1(b), SM Movie 1] [25]. At high frequencies (f > 25 Hz), the oscillation stage vanishes, and rollers run smoothly at a characteristic speed [Fig. 1(b), SM Movie 2]. Velocity increases with f except near 25 Hz, where motile behavior transitions [Fig. 1(c)]. A similar propulsion mechanism was employed to drive magnetic colloidal rollers immersed in liquid [13]. In contrast, our system uses larger granular rollers and operates in the absence of ambient liquid, where fluidmediated interactions are negligible. Notably, inertiaassisted self-propulsion drives a roller to move in the direction of its initial velocity. Consequently, collisions between rollers can alter the directions of both velocity and self-propulsion force. Moreover, after B is turned off, the running rollers continue to travel considerable distances (typically tens of d) due to inertia before stopping. These inertial rollers contrast sharply with asymmetric granular particles on a vibrating bed [17] and electric-powered Hexbugs [18,19], which stop immediately when energy input ceases.

Emergence of flocking phase separation—To investigate the emergence of collective motion, we confine rollers within a racetrack [Fig. 2(a)]. Collective motion emerges at high rollers' area fraction, ϕ . At low ϕ and f, rollers move randomly, forming an isotropic gaseous phase. When ϕ exceeds the threshold value at fixed f, the gaseous phase becomes unstable. A fraction of magnetic rollers self-organize into a dense flock, moving coherently either

clockwise or counterclockwise through a dilute gaseous phase of randomly moving particles [Fig. 2(a), SM Movies 3,4]. We characterize the two phases by measuring the local area fraction, $\phi(x)$, and mean tangential velocity field, $v(x) = \langle \mathbf{v}_i \rangle \cdot \mathbf{n}_x$ [25], over half period of $\mathbf{B}(t)$, where $x \in [0,1]$ is the curvilinear coordinate. Both $\phi(x)$ and v(x) are uniform separately within the flocking and gaseous phases, with an abrupt change at the interfaces [Fig. 2(b)]. Notably, the densities of the coexisting flocking and gaseous phases, ϕ_{flock} and ϕ_{gas} , are independent of ϕ . Increasing ϕ only elongates the flock length, L_f , following the lever rule [Fig. 2(c)]. We refer to this phase-separated phenomenon as "flocking phase separation" (FPS).

FPS, characterized by uniform flocking and gaseous phases with sharp interfaces [25], is observed across a wide range of parameters, as plotted in a phase diagram with respect to ϕ and f [Fig. 2(d)]. Both ϕ_{flock} and ϕ_{gas} decay rapidly with f at low f (< 25 Hz) and slowly at high f(>25 Hz), suggesting the influence of single-roller motility on collective motion. $\phi_{gas}(f)$ closely matches the onset density of FPS over all f. FPS is distinct from asymmetric solitary bands—characterized by a high-density front and a gradually decaying tail—observed in polar liquids composed by microscopic Quincke rollers [10], as well as from the delocalized density waves comprising multiple short bands found in dense motile filaments [30]. Although the three typical flocking patterns are predicted within the framework of the Toner-Tu theory [31], phase separation with uniform flocks has, to our knowledge, only been observed in simulations of the minimal active Ising model [32,33] and remains unreported experimentally. Moreover, the FPS is distinct from the well-known motility-induced phase separation (MIPS) of active Brownian particles [22], characterized by a dense stationary phase coexisting with a dilute, disordered phase lacking collective motion.

Dynamics of coexisting phases-As a new type of nonequilibrium phase separation, FPS exhibits a unique particle exchange process at the interfaces between coexisting phases. When a flock moves through the gaseous phase, particles at the forefront of the flock collide with those in the gas, which subsequently join the flock. Meanwhile, particles at the tail of the flock return to the gaseous phase, thereby maintaining a constant flock length. Consequently, the flock's propagation speed $v_{\rm flock}$ is greater than that of individual particles within the flock, v_{particle} [Fig. 2(e)]. Note that both v_{flock} and v_{particle} depend on driving frequency but are independent of ϕ . They follow the Rankine-Hugoniot jump condition $v_{\text{flock}} =$ $v_{\text{particle}}[(\phi_{\text{flock}}(f)/(\phi_{\text{flock}}(f)-\phi_{\text{gas}}(f))]$ [34], arising from particle number conservation. This relation indicates that the flock's forefront propagates as a shock wave, with the diffusion process being negligible. This is different from the situation in equilibrium systems, where diffusion plays a dominant role. We then examine number fluctuation

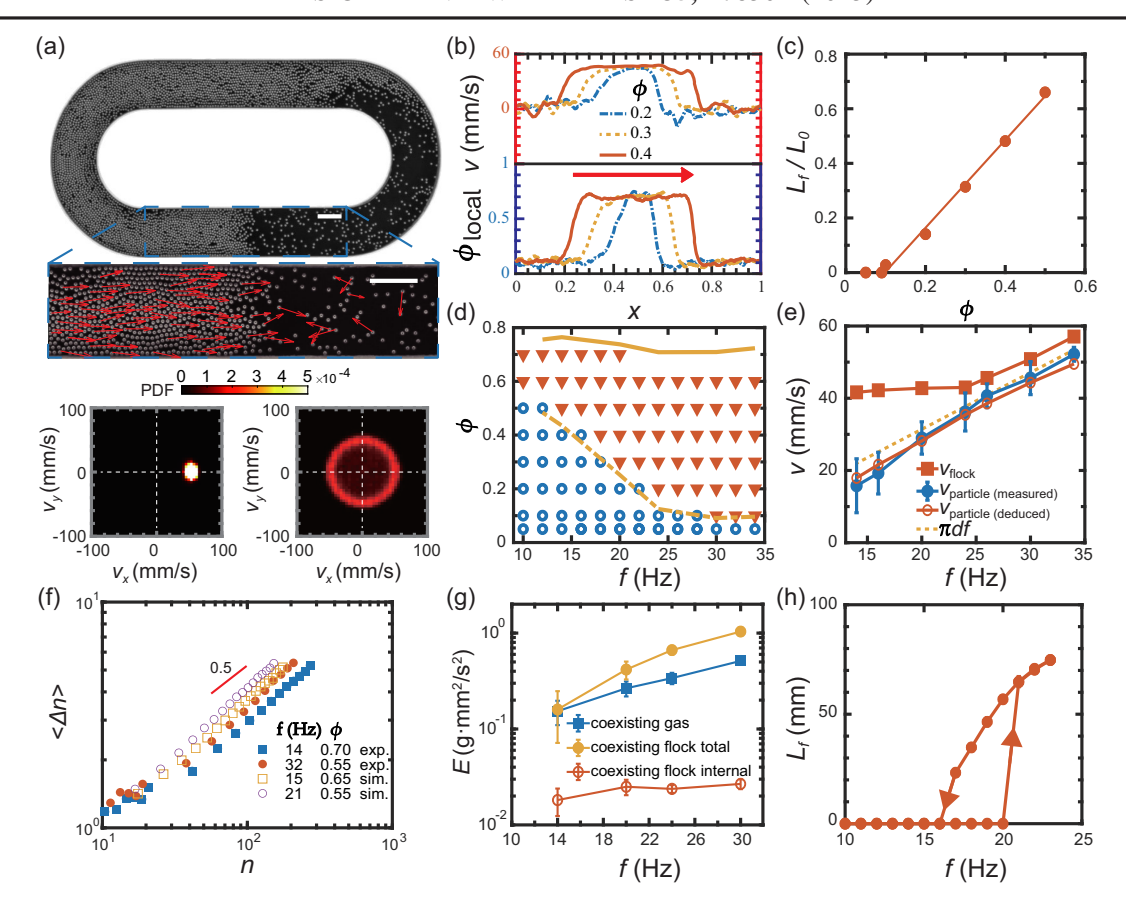


FIG. 2. (a) Snapshot of a flock propagating through an isotropic gaseous phase at f=34 Hz and $\phi=0.5$. Top: Near-field view highlighting two distinct phases within a straight section of the racetrack, with red arrows indicating local velocity. Scale bar: 5 mm. Bottom: Probability distribution of velocity (v) within the flock (left) and in the gaseous phase (right). (b) Spatial profiles of local particle velocity and area fraction measured along the curvilinear coordinate (x) at varying system area fractions $\phi=0.2$, 0.3 and 0.4, and fixed frequency f=30 Hz. (c) Reduced flock length (L_f/L_0) as a function of ϕ at f=30 Hz, where L_0 is the total racetrack length. (d) Phase diagram with respect to ϕ and f. Hollow circles denote isotropic states, while solid triangles indicate flocking phase separation. The dashed and solid lines represent $\phi_{\rm gas}(f)$ and $\phi_{\rm flock}(f)$ in the phase-separated state, respectively. (e) Propagation velocity of flocks $v_{\rm flock}$ (square), and particle velocity within flocks $v_{\rm particle}$ (circle). Since both $v_{\rm flock}$ and $v_{\rm particle}$ are independent of ϕ , the data are measured at various ϕ and averaged. Hollow circles represent velocities inferred from the Rankine-Hugoniot jump condition. The dashed line denotes the reference speed πdf . (f) Number fluctuations of the flock observed in experiments (solid symbols) and simulations (hollow symbols). (g) Energy per particle in the flocking and coexisting gaseous phases. Hollow symbols denote the internal kinetic energy within the flocking phase. Within each coexisting phase, E remains independent of Φ [25]; data are collected over a range of Φ values in the FPS regimes and subsequently averaged. (h) Hysteresis loop of flock length at $\Phi=0.41$, with arrows indicating the direction of temporal evolution.

within flocks in FPS, $\langle \Delta n \rangle = \sqrt{\langle n^2 \rangle - \langle n \rangle^2} \sim n^{\alpha}$, where n is the number of particles [25]. $\langle \Delta n \rangle$ is normal with $\alpha = 0.5$ [Fig. 2(f)]. This contrasts with previous studies on collective motion in other systems [17,35,36], which report giant number fluctuations with $\alpha > 0.5$.

Because of polar motion, flocking particles possess higher kinetic energy, $E=\frac{1}{2}M\langle \mathbf{v}_i^2\rangle$, than those in the coexisting gaseous phase [Fig. 2(g)]. To characterize relative particle motion within each phase, we measure the internal kinetic energy, $E^{\rm int}=\frac{1}{2}M\langle (\mathbf{v}_i-\langle \mathbf{v}\rangle)^2\rangle$. The internal energy corresponds to the effective temperature, $T=E^{\rm int}/k_B$, where k_B is the Boltzmann constant. In equilibrium systems, coexisting phases maintain equal temperatures. In contrast, the

dense flocking phase—despite containing faster-moving particles—exhibits a temperature an order of magnitude lower than that of the coexisting gaseous phase [Fig. 2(g)] due to strong coherent motion and suppressed random motion within the flock. A similar phenomenon has been reported in simulations of MIPS in inertial active Brownian particles [20,21], where the dilute phase also shows a higher temperature than the dense phase. These simulations attribute the temperature difference to particle inertia. However, direct experimental validation remains absent. In this Letter, we experimentally observe a temperature difference in an inertia-dominated, phase-separated active system. This feature differentiates phase separations in inertial active matter from those in equilibrium or overdamped active systems.

The presence of the lever rule governing the flock length in FPS suggests a first-order phase separation. To confirm this, we measure hysteresis by cycling f in a sample near the transition point [Fig. 2(h)]. As f is increased at 1 Hz/min, a flock with length $L_f=6.8$ mm emerges at 20 Hz, and L_f continues to increase with f. When f is decreased at the same rate, the flock gradually shrinks with f and disappears at 16 Hz. The finite hysteresis loop evidences the first-order nature of FPS.

Nucleation—To better understand the emergence of FPS, we examine how a flock nucleates from a supersaturated isotropic gas. Taking advantage of the tunable motility of rollers, we first set the system in an isotropic state and then increase f above the transition points. The system does not undergo phase separation immediately but exhibits an incubation period [Figs. 3(a)–3(e), SM Movie 5]. During the incubation period, rollers collide with their neighbors to form dense groups [Figs. 3(a) and 3(e)]. Most groups quickly disperse due to random motion of rollers, while a few temporarily move as flocks when rollers move in one direction. As a flock moves forward, rollers within the flock continuously collide with those in the gaseous phase. The flock will grow if it has sufficient momentum to convert these gaseous particles into part of the unidirectional flock. Otherwise, flocking rollers are scattered by randomly moving ones in the gaseous phase, causing the flock to shrink. A nucleus of the flocking phase forms from neighboring rollers with high local density and polar order. We track the evolution of nuclei and identify the critical nucleus, which has an equal probability of growing and shrinking [25] [Fig. 3(b)]. Its area fraction and particle velocity are much lower than ϕ_{flock} and v_{particle} in the steady

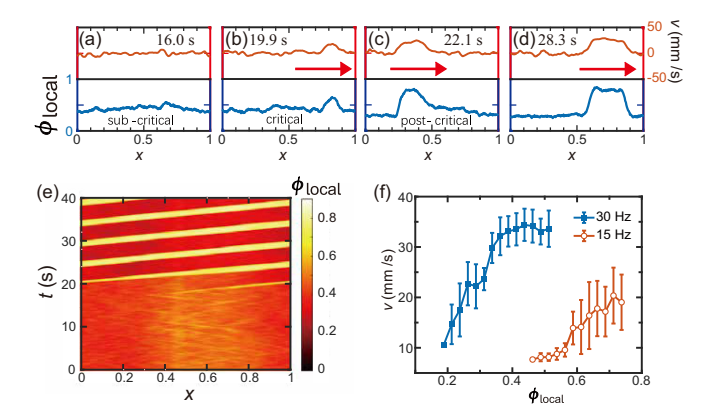


FIG. 3. (a)–(d) Snapshots of velocity (top) and density (bottom) profiles during nucleation and growth of a flock at f=15 Hz, $\phi=0.44$. The red arrows indicate propagation direction of the flock. A critical nucleus appears around 19.9 s (b). (e) Spatiotemporal evolution of area fraction along the curvilinear coordinate (x) during nucleation and growth of a flock at f=15 Hz and $\phi=0.44$. The color bar indicates the local area fraction. (f) Velocity-density relationship during nucleation and growth of flocks at 15 and 30 Hz in FPS.

state, respectively. The postcritical nucleus then becomes denser and longer by collecting particles from the gas [Fig. 3(c)], eventually growing into a steady flock after one or two laps around the racetrack [Fig. 3(d)]. During the nucleation and growth of the flocks, we find that the flock velocity increases with the flock density [Fig. 3(f)]. A faster-moving flock clearly facilitates the collection of particles from the gaseous phase, which in turn enhances its density. This creates a positive feedback loop that drives FPS, distinct from the positive feedback between higher density and lower motility in MIPS [22]. The emergence of FPS remains robust when the system size significantly exceeds the critical nucleus length [25].

Simulation and models—To elucidate the mechanism underlying the robust FPS in magnetic roller populations, we develop an agent-based simulation model that replicates the motion of magnetic rollers in a straight channel with periodic boundary conditions (Appendix A). Instead of neglecting physical details in minimal active models, our simulation explicitly identifies the self-propulsion mechanism of magnetic rollers and their interactions, including magnetic dipole interactions and direct collisions. The simulations accurately capture the key phenomena observed in both individual rollers and roller ensembles.

In a population of magnetic rollers, agents interact with their neighbors via magnetic interactions and inelastic collisions, which may contribute to the velocity alignment and particle condensation. To understand the roles of two interactions in governing FPS, we examine collective behaviors by "turning off" either magnetic dipole-dipole interaction or collision-induced energy dissipation in the simulation. Without magnetic dipole-dipole interactions, a stable flock still forms, retaining a structure similar to a regular flock. The absence of magnetic interactions does not impact the density profile or velocity profile, as shown by $\phi(x)$ and v(x) (Fig. 4), respectively. In contrast, without energy dissipation from collisions, FPS fails, resulting in a fluctuating $\phi(x)$ and v(x) around zero across the channel. Thus, inelastic collisions between rollers alone induce the alignment of rollers and then the formation of a flock. Specially, the inelastic collisions between rollers reduce their relative velocities and lead to their velocities converging [25] (SM Movie 6). Then the inertia-assisted selfpropulsion reaccelerates the colliding particles and makes them roll along similar direction.

Finally, we use the celebrated Toner-Tu theory to investigate the emergence of the flocking phase separation. In the framework of this continuum theory, the key ingredients for inducing the FPS are the positive feedback between high density and polar motion, quantified by the intrinsic velocity-density relation, $v(\phi)$. We obtain this function by simulating roller populations in a short periodic channel, where the system keeps in metastable uniform state rather than phase-separated state, and then by calculating the global average velocity (Appendix B). This

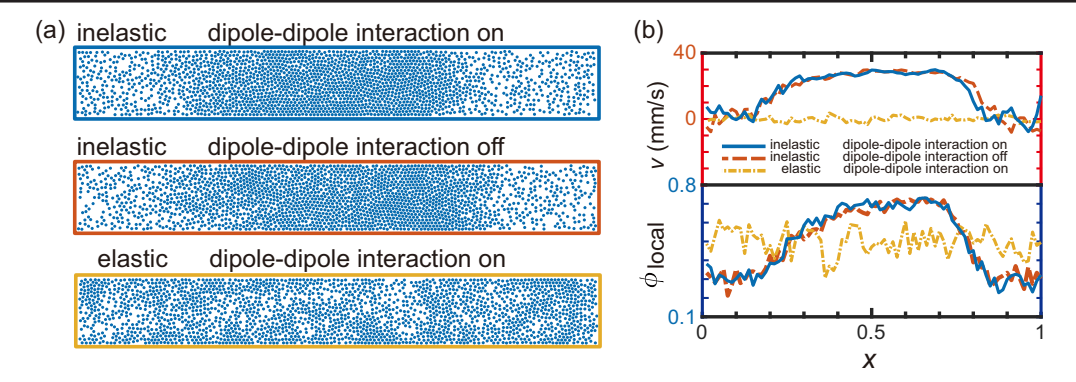


FIG. 4. (a) Simulation snapshots of roller populations at f = 22 Hz and $\phi = 0.5$ under three interaction scenarios: (i) inelastic collisions with magnetic dipole-dipole interactions (blue box), (ii) inelastic collisions without dipole-dipole interactions (red box), and (iii) elastic collisions with dipole-dipole interactions (yellow box). (b) Profiles of velocity and local area fraction measured along the curvilinear coordinate, x, for the three interaction scenarios. The color code is the same as in (a).

approach establishes a link between the agent-based model and the continuum description, with agent-level effects captured by the velocity-density relation $v(\phi)$. The velocity $v(\phi)$ is zero at low density and becomes positive above a threshold area fraction [Fig. 6(a)], indicating symmetry breaking and the onset of polar order. Further simulations show that both inertia and collisional energy dissipation are essential for obtaining a nontrivial $v(\phi)$ [25]. By solving the one-dimensional Toner-Tu equation with $v(\phi)$ and fluctuations, we find that FPS emerges from a uniform supersaturated state via a nucleation process with key features observed in experiments (Appendix B). The influence of motile behaviors is reflected in $v(\phi)$, which determines the densities of two coexisting phases. Previous simulation studies show that flocking pattern selection depends on number fluctuations: phase separation is stable for normal number fluctuations in the active Ising model, whereas giant number fluctuations correlate with microphase separation in the Vicsek model [31,37]. Normal number fluctuations observed in our experiments and agent-based simulations confirm the pattern selection rule [Fig. 2(f)].

Conclusion—Taken together, we propose a macroscopic model system consisting of numerous motility-tunable magnetic rollers, in which flocking emerges as a first-order phase separation characterized by a uniform bulk and sharp interfaces. The FPS results from inelastic collisions between field-driven inertial rollers, which create positive feedback between high local density and strong polar motion. The population of magnetic rollers holds potential as an ideal platform to reveal large-scale collective behaviors of inertial dry active matter at the single-particle level. Systematic control over their motile behaviors, pair interactions, and confining boundaries will enhance our understanding of collective motion in complex systems. This research may pave the way for developing new strategies to manipulate animal flocks [38], traffic dynamics [7,39], and robotic swarms [6,8,9].

Acknowledgments—This work was supported by the National Natural Science Foundation of China No. 12474206 and No. 12074406 (Y. P.), No. T2325027 and No. 12274448 (M. Y.), National Key R&D Program of China 2022YFF0503504 (M. Y.), and Chinese Academy of Sciences.

Data availability—The data that support the findings of this article are openly available [40].

^[1] M. C. Marchetti, J. F. Joanny, S. Ramaswamy, T. B. Liverpool, J. Prost, M. Rao, and R. A. Simha, Rev. Mod. Phys. **85**, 1143 (2013).

^[2] C. Bechinger, R. Di Leonardo, H. Löwen, C. Reichhardt, G. Volpe, and G. Volpe, Rev. Mod. Phys. **88**, 045006 (2016).

^[3] S. Shankar, A. Souslov, M. J. Bowick, M. C. Marchetti, and V. Vitelli, Nat. Rev. Phys. 4, 380 (2022).

^[4] T. Vicsek and A. Zafeiris, Phys. Rep. 517, 71 (2012).

^[5] J. Buhl, D. J. Sumpter, I. D. Couzin, J. J. Hale, E. Despland, E. R. Miller, and S. J. Simpson, Science 312, 1402 (2006).

^[6] M. Rubenstein, A. Cornejo, and R. Nagpal, Science 345, 795 (2014).

^[7] J. Aguilar, D. Monaenkova, V. Linevich, W. Savoie, B. Dutta, H.-S. Kuan, M. D. Betterton, M. A. D. Goodisman, and D. I. Goldman, Science **361**, 672 (2018).

^[8] S. Li, R. Batra, D. Brown, H.-D. Chang, N. Ranganathan, C. Hoberman, D. Rus, and H. Lipson, Nature (London) 567, 361 (2019).

^[9] B. Saintyves, M. Spenko, and H. M. Jaeger, Sci. Robot. 9, eadh4130 (2024).

^[10] A. Bricard, J.-B. Caussin, N. Desreumaux, O. Dauchot, and D. Bartolo, Nature (London) 503, 95 (2013).

^[11] J. Palacci, S. Sacanna, A. P. Steinberg, D. J. Pine, and P. M. Chaikin, Science 339, 936 (2013).

^[12] Y. Goto and H. Tanaka, Nat. Commun. 6, 5994 (2015).

^[13] A. Kaiser, A. Snezhko, and I. S. Aranson, Sci. Adv. 3, e1601469 (2017).

^[14] Z. Shen and J. S. Lintuvuori, Phys. Rev. Lett. **125**, 228002 (2020).

- [15] Z. Shen and J. S. Lintuvuori, Phys. Rev. Lett. 130, 188202 (2023).
- [16] P. Chen, S. Weady, S. Atis, T. Matsuzawa, M. J. Shelley, and W. T. Irvine, Nat. Phys. 21, 146 (2024).
- [17] V. Narayan, S. Ramaswamy, and N. Menon, Science 317, 105 (2007).
- [18] O. Dauchot and V. Démery, Phys. Rev. Lett. 122, 068002 (2019).
- [19] Y. Xia, Z. Hu, D. Wei, K. Chen, Y. Peng, and M. Yang, Phys. Rev. Lett. 133, 048302 (2024).
- [20] S. Mandal, B. Liebchen, and H. Löwen, Phys. Rev. Lett. 123, 228001 (2019).
- [21] L. Hecht, S. Mandal, H. Löwen, and B. Liebchen, Phys. Rev. Lett. 129, 178001 (2022).
- [22] M. E. Cates and J. Tailleur, Annu. Rev. Condens. Matter Phys. 6, 219 (2015).
- [23] D. Geyer, D. Martin, J. Tailleur, and D. Bartolo, Phys. Rev. X 9, 031043 (2019).
- [24] J. Zhang, R. Alert, J. Yan, N. S. Wingreen, and S. Granick, Nat. Phys. 17, 961 (2021).
- [25] See Supplemental Material http://link.aps.org/supplemental/ 10.1103/hb7b-wp95 for additional information about the experimental methods and extended discussion, which includes Refs. [26–29].
- [26] R. C. Hibbeler, *Engineering Mechanics. Statics*, 14th ed. (Pearson Prentice Hall, Hoboken, N.J, 2016).
- [27] A. Zöttl and H. Stark, Annu. Rev. Condens. Matter Phys. 14, 109 (2023).

- [28] J. C. Crocker and D. G. Grier, J. Colloid Interface Sci. 179, 298 (1996).
- [29] J. Wedekind, R. Strey, and D. Reguera, J. Chem. Phys. 126, 134103 (2007).
- [30] V. Schaller, C. Weber, C. Semmrich, E. Frey, and A. R. Bausch, Nature (London) 467, 73 (2010).
- [31] J.-B. Caussin, A. Solon, A. Peshkov, H. Chaté, T. Dauxois, J. Tailleur, V. Vitelli, and D. Bartolo, Phys. Rev. Lett. 112, 148102 (2014).
- [32] A. P. Solon and J. Tailleur, Phys. Rev. Lett. 111, 078101 (2013).
- [33] S. Mishra, A. Baskaran, and M. C. Marchetti, Phys. Rev. E 81, 061916 (2010).
- [34] D. J. Acheson, Elementary Fluid Dynamics (Oxford University Press, Oxford, 1990).
- [35] D. Geyer, A. Morin, and D. Bartolo, Nat. Mater. 17, 789 (2018).
- [36] Y. Peng, L. Lai, Y.-S. Tai, K. Zhang, X. Xu, and X. Cheng, Phys. Rev. Lett. 116, 068303 (2016).
- [37] A. P. Solon, H. Chaté, and J. Tailleur, Phys. Rev. Lett. 114, 068101 (2015).
- [38] D. J. Sumpter, Collective Animal Behavior (Princeton University Press, Princeton, NJ, 2010).
- [39] D. Helbing, Rev. Mod. Phys. 73, 1067 (2001).
- [40] N. Luo, L. Li, M. Yang, and Y. Peng, Dataset for "Flocking phase separation in inertial active matter" (2025), 10.6084/m9.figshare.30239644.
- [41] M. Han, M. Fruchart, C. Scheibner, S. Vaikuntanathan, J. J. De Pablo, and V. Vitelli, Nat. Phys. 17, 1260 (2021).
- [42] Y. Tu, J. Toner, and M. Ulm, Phys. Rev. Lett. 80, 4819 (1998).

End Matter

Appendix A—An agent-based simulation model is introduced to mimic the motion of magnetic rollers. We consider an ensemble of magnetized spheres, characterized by a diameter d, mass M, and moment of inertia $I = Md^2/10$, rolling on a substrate in the xy plane. These particles are confined in a two-dimensional channel of width w and length l, with the periodic boundary conditions along the x direction and wall boundaries in the y direction. The entire system is subjected to a time-varying magnetic field, $\mathbf{B}(t) = B_0 \mathrm{sgn}[\sin(2\pi ft)]\hat{\mathbf{e}}_z$, where f denotes the frequency, "sgn" represents the sign function, and $\hat{\mathbf{e}}_z$ is unit vector along the z axis. Under this oscillating magnetic field, the magnetized particles are driven to rotate. The frictional force between the substrate and particles converts this rotation into net rolling motion.

Specifically, the dynamic equation of particle i with position \mathbf{r}_i and angular velocity $\boldsymbol{\omega}_i$ is modeled as

$$M\ddot{r}_{i} = f_{i}^{w} + f_{i}^{s} + \sum_{j \in N_{i}^{c}} f_{ij}^{c} + \sum_{j \in N_{i}^{m}} f_{ij}^{m}$$
 (A1)

$$I\dot{\boldsymbol{\omega}}_{i} = \boldsymbol{T}_{i}^{e} + \boldsymbol{T}_{i}^{r} + \frac{d}{2}\boldsymbol{f}_{i}^{s} \times \hat{\boldsymbol{e}}_{z} + \sum_{j \in N_{i}^{c}} \boldsymbol{f}_{ij}^{c} \times \boldsymbol{r}_{ij} + \sum_{j \in N_{i}^{m}} \boldsymbol{T}_{ij}^{m} + \zeta_{i}\hat{\boldsymbol{e}}_{z}.$$
(A2)

Here, f_i^w represents the volume exclusion force exerted by the channel wall, and f_i^s denotes the frictional force applied by the substrate. Based on experimental observations, f_i^s is modeled as static friction up to a maximum value, f_M^s , beyond which it transitions to sliding friction, i.e., $|f_i^s| \le f_M^s$. f_{ij}^c (f_{ij}^m) represents the force arising from collisions (magnetic dipole-dipole interactions) between particle i and its neighbors $j \in N_i^c$ $(j \in N_i^m)$ when their separation distance $r_{ij} < r_c = 2^{1/12}d$ $(r_{ij} < r_m = 5d)$. Note that the collision force f_{ij}^c includes three contributions: the volume exclusion, friction effect, and inelastic collision. For simplicity, this Letter models all volume exclusion using a truncated and shifted Lennard-Jones type potential: $U(r) = 4\epsilon [(d/r)^{24} - (d/r)^{12}] + \epsilon$ with interaction strength $\epsilon = 0.1$ if $r < r_c$, and U(r) = 0 otherwise. The effect of friction and inelastic collision is constructed by the relative velocities between particles, as done in Ref. [41]. As a result, the collision force is given by

$$f_{ij}^c = -\nabla_{\mathbf{r}_{ij}} U - \gamma (\mathbf{v}_{ij} - \boldsymbol{\omega}_{ij} \times \mathbf{r}_{ij}), \tag{A3}$$

with the vector along the direction from particle j to i, $\mathbf{r}_{ij} = \mathbf{r}_i - \mathbf{r}_j$, their relative velocity, $\mathbf{v}_{ij} = \mathbf{v}_i - \mathbf{v}_j$, and the average rotational velocity $\boldsymbol{\omega}_{ij} = (\boldsymbol{\omega}_i + \boldsymbol{\omega}_j)/2$. The term

 $\gamma(\boldsymbol{v}_{ij} - \boldsymbol{\omega}_{ij} \times \boldsymbol{r}_{ij})$ captures both the interparticle tangential friction and dissipative normal forces during collisions, with γ the inelastic collision coefficient. Moreover, the force induced by dipole-dipole interactions follows $f_{ij}^m = \nabla_{\boldsymbol{r}_{ij}}(\boldsymbol{m}_i \cdot \boldsymbol{B}_j)$, where $\boldsymbol{B}_j = (\mu_0/4\pi)[3\boldsymbol{r}_{ij}(\boldsymbol{r}_{ij} \cdot \boldsymbol{m}_j) - |\boldsymbol{r}_{ij}|^2\boldsymbol{m}_j]/|\boldsymbol{r}_{ij}|^5$ is the magnetic field generated by the magnetic dipole \boldsymbol{m}_j at the location of particle i.

In Eq. (A2), $T_i^e = m_i \times B$ and $T_{ij}^m = m_i \times B_j$ denote the torque on particle i produced by the time-varying magnetic filed B and the dipole-induced magnetic filed B_i , respectively. The terms $d\mathbf{f}_{i}^{s} \times \hat{\mathbf{e}}_{z}/2$ and $\mathbf{f}_{ij}^{c} \times \mathbf{r}_{ij}$ separately account for the torque arising from frictional force (between particle i and substrate) and collision force (between particle i and j). Additionally, $T_i^r = -[T_M^r \omega_{ix}/$ $|\boldsymbol{\omega}_i \times \hat{\boldsymbol{e}}_z|, T_M^r \omega_{iy}/|\boldsymbol{\omega}_i \times \hat{\boldsymbol{e}}_z|, T_M^f \omega_{iz}/|\omega_{iz}|]$ describes the effects of rolling resistance [26] and friction, in which T_M^r and T_M^J represent the resisting torque and frictional torque, respectively, and ω_{ix} , ω_{iy} , and ω_{iz} are the components of ω_i . Finally, to mimic the perturbation of rough substrate in the rolling direction of particles, Gaussiandistribution stochastic torque ζ_i is introduced in the z direction, satisfying $\langle \zeta_i \rangle = 0$ and $\langle \zeta_i(t)\zeta_i(t') \rangle =$ $D_r\delta(t-t')$.

In our simulation, we adopt the particle's diameter d, mass M, and magnetic dipole moment m_0 as the units of length, mass, and magnetic moment, respectively. The unit of time t is set to 10^{-3} s. Based on experimental

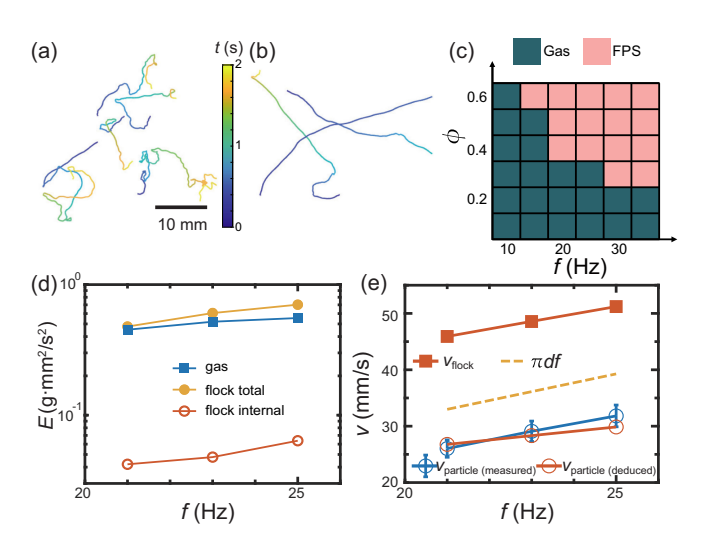


FIG. 5. Simulated single-roller trajectories at 10 Hz (a) and 30 Hz (b), with the color bar indicating elapsed time. (b) Phase diagram obtained from the simulation results, showing the phase boundary consistent with experimental observation. (d) Energy per particle of two phases observed in simulations. (e) Propagation velocity of flocks $v_{\rm flock}$ (square), and particle velocity within flocks $v_{\rm particle}$ (circle) in simulations. They follow the Rankine-Hugoniot jump condition.

parameters, we take the channel size as $w \times l = 20 \times 160$, corresponding to the area fraction $\phi = N\pi/12\,800$ with the number of particle N. The amplitude of time-varying magnetic field is $B_0 = 7.1 \times 10^{-3}$, and the permeability of vacuum is $\mu_0 = 1.8 \times 10^{-3}$. The collision coefficient between particles is $\gamma = 0.1$. For the interaction between particle and substrate, we set the maximum static friction force $f_M^s = 5 \times 10^{-3}$, the resisting torque $T_M^r = 5 \times 10^{-5}$, and the frictional torque $T_M^f = 0.1 T_M^r$. Additionally, noise strength is given by $\sqrt{D_r} = 3.2 \times 10^{-3}$.

The single roller exhibits run-and-oscillate and smoothrun behaviors at low and high frequencies, respectively [Figs. 5(a) and 5(b)]. The simulated rollers display qualitatively the same collective behaviors as experimental results [Figs. 5(c)-5(e)].

Appendix B—We employ a one-dimensional stochastic Toner-Tu model with density-dependent parameters to account for density-enhanced velocity [31,42],

$$\partial_t \phi + \partial_x W = D_\phi \partial_{xx} \phi, \tag{B1}$$

$$\partial_t W + \xi W \partial_x W = a_2(\phi) W - a_4 W^3 - \partial_x P(\phi) + D_W \partial_{xx} W + \eta.$$
(B2)

Here, $\phi(x,t)$ and $W(x,t) = \phi(x,t) \cdot v(x,t)$ represent the density and momentum fields, respectively. The parameters $\xi, \lambda, a_4, D_\phi, D_W$ are positive constants, while η denotes zero-mean Gaussian white noise. For simplicity, we assume a linear pressure relation, $P(\phi) = \lambda \phi$. At lower densities, where $a_2(\phi) < 0$, the system resides in an disordered phase. At higher densities, where $a_2(\phi) > 0$, the system exhibits a trivial polarized solution: $\phi(x,t) = \phi_0, \quad W(x,t) = \pm \sqrt{[a_2(\phi_0)/a_4]}$. The trivial solution corresponds to a metastable uniform state.

While previous studies typically assume a_2 to be a simple function of ϕ [31], we aim to derive $a_2(\phi)$ directly from the dynamics of the magnetic roller system. We obtain the velocity-density relation $v(\phi)$ by simulating a roller assembly at densities ϕ in a short channel (l = 25) with periodic boundary conditions, where the system remains in a uniform state—rather than undergoing FPS—due to finite-size effects. For each pair (ϕ, f) , particles are initialized with random positions and velocities. Simulations are run for at least 1000 magnetic periods. During relaxation, we monitor the velocity v(t) = $\langle \boldsymbol{v}(x,t) \rangle \cdot \boldsymbol{n}_{x}$, where \boldsymbol{n}_{x} is the tangential unit vector along the channel centerline, and the average is taken over all particles. Once v(t) stabilizes, we collect instantaneous roller velocities over 100 magnetic periods and compute the mean velocity v via time and ensemble averaging. We repeat simulations for various densities ϕ to construct the $v(\phi)$ curve. To test FPS at various frequencies, we simulate three sets of $v(\phi)$ for f = 15, 22, and 29 Hz [Fig. 6(a)].

In addition, the curve $v(\phi)$ is fitted using the following functional form:

$$v(\phi) = \begin{cases} 0 & \phi < B \\ A\sqrt{\phi - B} & B < \phi < E \\ -C\phi + D & E < \phi < D/C. \end{cases}$$
 (B3)

Here, [A, B, C, D] are fitting parameters and E denotes the smaller intersection point of $v(\phi) = A\sqrt{\phi - B}$ and $v(\phi) = -C\phi + D$. For f = 15, 22, and 29 Hz, the corresponding parameter sets are [39.9, 0.55, 350, 280], [53.3, 0.39, 590, 472], and [68.8, 0.30, 403, 326], respectively. For $\phi > \phi_s$, $a_2(\phi)$ is given by $a_2(\phi) = a_4W^2(\phi) = a_4\phi^2v^2(\phi)$, where ϕ_s is the density threshold above which the coarse-grained velocity $v(\phi)$ becomes positive. The parameter $a_4 = 30$ is chosen to match the characteristic duration of a roller flip under the alternating current magnetic field. For $\phi < \phi_s$, $a_2(\phi)$ decreases linearly from 0 at ϕ_s to $-a_4$ at $\phi = 0$.

For simplicity, the spatial coordinate x is rescaled by dividing it by πdf , ensuring $W \in [0,1]$. Consistent with Ref. [23], we set $\xi=1$. The noise strength $\sigma_{\eta}=0.03$ is inferred from the variation in the simulated collective velocity [Fig. 6(a)]. Additionally, the linear pressure parameter is set as $\lambda=1$, while the diffusion parameters are $D_{\phi}=D_{W}=0.1$. All calculations are performed using PYTHON with the PY-PDE library. The system size is $L_{0}=20$, the grid spacing $\Delta x=0.1$, and the time step $\Delta t=0.0005$. Using these parameters, we solve the 1D Toner-Tu model in a supersaturated homogeneous system. FPS emerges via a nucleation process and reaches the

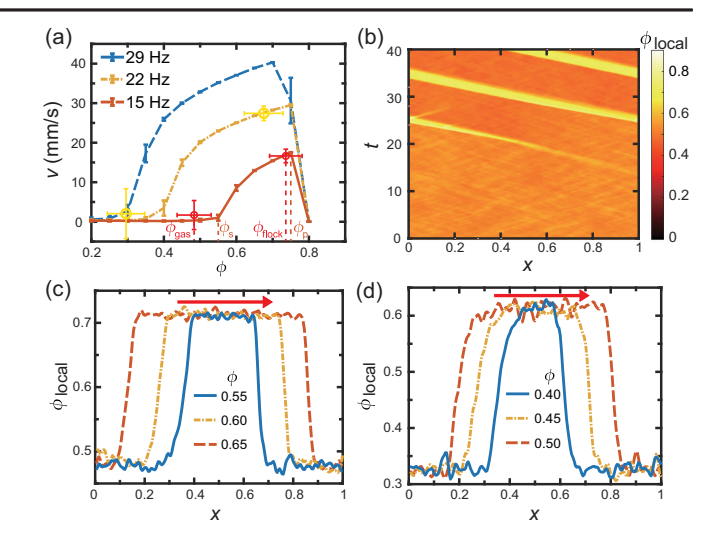


FIG. 6. (a) Velocity-density relationships obtained from simulations in uniform and metastable states at 15, 22, and 29 Hz. The agent-based simulation is performed in a short-channel configuration, preventing phase separation and maintaining uniformity. Red and yellow symbols indicate the densities of two phases obtained directly from the simulation at 15 and 22 Hz. ϕ_s and ϕ_p are defined as where $v(\phi)$ starts to increase and reaches the peak, respectively. ϕ_s and ϕ_p are closed to $\phi_{\rm gas}$ and $\phi_{\rm flock}$, respectively. (b) Spatiotemporal profile of local area fraction calculated within the Toner-Tu theory framework using the velocity-density relationship from (a) at 22 Hz. Toner-Tu theory predicts uniform density profiles within flocks at 15 Hz (c) and 22 Hz (d). The red arrow indicates the propagation direction of flocks.

steady state [Fig. 6(b)]. The steady flocks exhibit uniform density [Figs. 6(c) and 6(d)] and follow the lever rule, as observed in the experiments.